The Dual-Current Control Strategy of Grid-Connected Inverter With *LCL* Filter

Yuanpeng Guan, Yu Wang, Yunxiang Xie, Yi Liang, Anna Lin, and Xuemei Wang, *Member, IEEE*

***Abstract*—In the renewable energy generation systems, the grid-connected inverter with *LCL* filter (GCI-*LCL*) is an important device to realize dc–ac power conversion and connect the distributed power generation system and power grid. However, the resonance problems of the *LCL* filter may bring instability to GCI-*LCL*. Besides, the grid impedance and the time delay in digital controllers also have a harmful influence on the stability of GCI-*LCL*. To solve these problems, a dual-current active damping control strategy based on the inverter-side current and grid-connected current feedback for GCI-*LCL* is proposed in this paper, and the systematic parameters design process is investigated. Compared with the conventional damping strategies, a resonance suppression for the *LCL* filter, a larger stability margin, and a better anti-interference capability in a weak grid can be achieved under the proposed strategy. In addition, by analyzing the active damping effect of the proposed strategy, a simplified model in a low-frequency band for GCI-*LCL* is proposed to enhance the anti-interference capability in the weak grid and simplify the parameters design process. Finally, a GCI-*LCL* prototype is constructed and the experiment results verify the correctness and feasibility of the analysis and proposed strategy.**

***Index Terms*—Anti-interference capability, dual-current control strategy, grid-connected inverter with LCL filter (GCI-LCL), resonance suppression, stability margin.**

NOMENCLATURE

C	Capacitor in the *LCL* filter.
f_{LCL}	Resonance frequency of the *LCL* filter.
f_n	Fundamental frequency.
f_S	Switching frequency.
GCI	Grid-connected inverter.
GCI-*LCL*	Grid-connected inverter with *LCL* filter.
G_D	Whole time delay model.
G_i	PI controller.
G_{inv}	Transfer function from u_{inv} to i_2.
GM	Gain margin.
i_1	Inverter-side current.
i_{2o}	Grid-connected current in the open loop.

Manuscript received August 1, 2018; accepted September 3, 2018. Date of publication September 9, 2018; date of current version April 20, 2019. This work was supported by the National Natural Science Foundation of China under Grant 51577074. Recommended for publication by Associate Editor H. H.-C. Iu. *(Corresponding author: Yu Wang.)*

Y. Guan, Y. Xie, Y. Liang, A. Lin, and X. Wang are with the School of Electric Power, South China University of Technology, Guangzhou 510641, China (e-mail:

To eliminate the high-frequency harmonics generated by operation of the GCI, a filter is generally installed between the GCI and power grid. Compared with the L-type filter, the *LCL* filter has a better high-frequency harmonic attenuation capability, a smaller inductance, and a higher power density. Therefore, the *LCL*-type filter is usually applied [5], [6]. However, the *LCL* filter is a third-order system with resonance problem that causes oscillation and instability for the GCI. Fortunately, the problem can be solved with varieties of strategies, including the passive damping method [7], [8], active damping method [9]–[12], model-based reduce-order method [13], [14], and additional filter method [15], [16]. Due to the large power loss in passive damping resistance, the passive damping method is often replaced by other methods. Besides, the model-based reduce-order method mainly contains the splitting capacitor method and weighted current method, and they are sensitive to parameters perturbation. Moreover, the additional filter method is achieved with an ideal damping performance by designing filters including a notch filter, a lead-lag compensator, or a quadratic filter, and it is a high-order system that its parameters design process is complicated. The active damping method suppresses the resonance through the state variables feedback, including

1) capacitor current and grid-connected current feedback;
2) capacitor current and inverter-side current feedback;
3) capacitor voltage and grid-connected current feedback;
4) capacitor voltage and inverter-side current feedback;
5) full-state variables feedback.

The state variables feedback strategies based on capacitor current or capacitor voltage increase the damping of GCI-*LCL*. However, in the capacitor voltage feedback strategy, a better effect can be obtained by the differential link, which is difficult to realize in a digital signal processor (DSP). Besides, in the capacitor current feedback strategy, the detection of a high-frequency current generates high cost from the current transformers, collectors, and DSP. In addition, the full-state feedback can rebuild a new damping model to gain a better damping effect. However, it requires more sensors, thus increasing the control complexity and cost. Moreover, the full-order observer and reduced-order observer benefit from reduced sensors based on an accurate model of the *LCL* filter. However, they are interfered by the grid impedance [17], [18]. Furthermore, the above-mentioned methods seldom focus on both the protection of switches in bridges and the grid-connected characteristics.

The grid impedance and *LCL* filter disturbance bring challenges in the stability of GCI-*LCL* and the grid-connected characteristics including the filtering and damping characteristic, stability margin, and power factor (PF) [19]–[24]. Moreover, the time delay caused by the one sampling period time delay, the sampler, and the zero-order hold also has an influence on the GCI-*LCL*'s stability and deteriorates the filtering characteristic [25]–[30]. To solve the problems, a numerous time-delay compensation method based on a model-free delay compensation is proposed [25]. However, the compensator is an IIR digital filter, which increases the system order, and the compensator design is difficult with the influence of a weak grid. In [26] and [27], the digital controller is designed with the determination of resonance frequency. However, the controller design becomes more complex with the uncertainty of the weak grid. In [28], the resonance frequency is limited under 1/6 f_s to ensure the stability of GCI-*LCL*. However, its controller parameters were designed without time delay. In [29], the controller parameters are determined considering time delay. However, the design process considering stability factors is complicated. In [30], the equivalent effect between virtual damping model and passive damping model is applied to simplify the design process. However, its optimal damping residence needs to be designed in advance.

Considering the above disadvantages in the existing damping strategies, a dual-current feedback control strategy based on the inverter-side current and grid-connected current feedback is proposed for GCI-*LCL* in this paper. The inverter-side current feedback provides the resonance suppression for GCI-*LCL* and improves quality of the inverter-side current to protect switches in bridges. Then, a simplified model in a low-frequency band based on the inverter-side current feedback is proposed to simplify the parameters design process. The grid-connected current feedback benefits the grid-connected characteristics and controller design. The systematic parameters design process of the proposed strategy, considering the resonance suppression, stability margin, and grid-connected characteristics, is presented to ensure the stable operation of GCI-*LCL* under the weak grid. Comparing with the previous works, the GCI-*LCL* under the proposed strategy achieves an ideal resonance suppression and a larger stability margin, and ensures the robustness of GCI-*LCL* and better grid-connected characteristics under the weak grid.

The rest of this paper is organized as follows. In Section II, the dual-current feedback control strategy based on the inverter-side current and grid-connected current feedback is proposed, and its mathematical model with time delay is established. In Section III, the systematic parameters design of the proposed strategy is discussed. In Section IV, a case study under the proposed strategy and its systematic parameters design process is investigated, and the comparison between the proposed strategy and conventional control strategies under the weak grid is presented. In Section V, the experiments results verify the correctness and feasibility of the analysis and proposed strategy. Finally, a conclusion is drawn in Section VI.

II. Dual-Current Control Strategy of GCL-*LCL* and Its Mathematical Model

The configuration of GCI-*LCL* under the proposed dual-current control strategy is depicted in Fig. 1. The inverter-side inductance L_1, the capacitor C, and the grid-side inductance L_2 constitute the *LCL* filter. The grid impedance is equivalent as an inductance L_g. i_1, i_2, and i_c are the inverter-side current, grid-connected current, and capacitor current, respectively. $U_{\rm dc}, u_{\rm inv}, u_c$, and u_g are the dc-side voltage, inverter-side voltage, capacitor voltage, and grid voltage, respectively. The PLL provides the phase of grid voltage at PCC to ensure the reference current in sync with grid voltage. The proposed dual-current control strategy is based on inverter-side current and grid-connected current feedback. The grid-connected

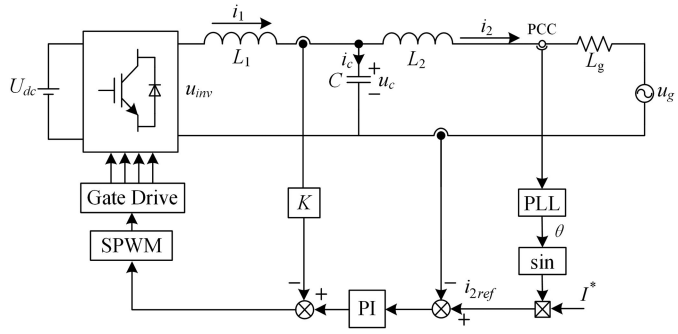

Fig. 1. Configuration of GCI-*LCL* under the proposed dual-current control strategy.

current feedback is the outer current close loop to trace the reference current by a PI controller in the ABC coordinate, thus satisfying the requirements of PF and total harmonic distortion (THD). Besides, the inverter-side current feedback through feedback parameter K is the inner loop to improve the resonance suppression effect, stability margin, and anti-interference capability. Then, the signal is modulated by a sinusoidal pulsewidth modulation (SPWM) strategy to gate drivers in switches.

From Fig. 2, the transfer function of the *LCL* filter from inverter-side voltage u_{inv} to grid-connected current i_2 is

$$G_{LCL}(s) = \frac{i_2}{u_{\text{inv}}} = \frac{1}{L_1 L_2 C s^3 + (L_1 + L_2)s}. \tag{1}$$

The resonance frequency f_{LCL} of the *LCL* filter can be expressed as

$$f_{LCL} = \frac{1}{2\pi}\sqrt{\frac{L_1 + L_2}{L_1 L_2 C}}. \tag{2}$$

Without considering the time delay, the equivalent block diagram of GCI-*LCL* under the proposed strategy is shown in Fig. 2(a). The open- and close-loop transfer functions with PI controller and grid voltage u_g are described as (3) and (4) shown at the bottom of this page.

$$G_i(s) = K_P + \frac{K_I}{s} \tag{5}$$

where G_i is the transfer function of the PI controller, and Δi_{2_g} and i_{2_i} are the interference current caused by grid voltage and grid-connected current.

Considering the time delay, the equivalent block diagram of GCI-*LCL* under the proposed strategy is shown in Fig. 2(b). The one sampling period time delay is e^{-sT_S}, the sampler is $1/T_S$, the zero-order holder is $(1 - e^{-sT_S})/s$, and the open- and close-loop transfer functions with PI controller and grid voltage u_g are described as (6) and (7) shown at the bottom of this page.

$$G_D(s) = \frac{1}{T_S} e^{-sT_S} \frac{1 - e^{-sT_S}}{s} \approx e^{-1.5sT_S} \tag{8}$$

where G_D is the whole time delay, and Δi_{2_gD} and i_{2_iD} are the interference current caused by grid voltage and grid- connected current with time delay.

$$\begin{aligned} i_{2o}(s) = {} & \frac{K_{\text{PWM}}}{L_1(L_2+L_g)Cs^3 + C(L_2+L_g)KK_{\text{PWM}}s^2 + (L_1+L_2+L_g)\,s + KK_{\text{PWM}}} \times G_i i_{2\text{ref}} \\ & - \frac{s^2 L_1 C + sCK_{\text{PWM}}K + 1}{s^3 L_1(L_2+L_g)C + C(L_2+L_g)KK_{\text{PWM}}s^2 + s\,(L_1+L_2+L_g) + KK_{\text{PWM}} + K_{\text{PWM}}G_i} \times u_g \end{aligned} \tag{3}$$

$$\begin{aligned} i_{2c}(s) = {} & i_{2c\_i} + \Delta i_{2c\_g} \\ = {} & \frac{K_P K_{\text{PWM}} s + K_I K_{\text{PWM}}}{L_1\,(L_2+L_g)\,Cs^4 + C(L_2+L_g)KK_{\text{PWM}}s^3 + (L_1+L_2+L_g)\,s^2 + (K_P+K)\,K_{\text{PWM}}s + K_I K_{\text{PWM}}} i_{2\text{ref}} \\ & - \frac{L_1 Cs^3 + CKK_{\text{PWM}}s^2 + s}{L_1\,(L_2+L_g)\,Cs^4 + C(L_2+L_g)KK_{\text{PWM}}s^3 + (L_1+L_2+L_g)\,s^2 + (K_P+K)\,K_{\text{PWM}}s + K_I K_{\text{PWM}}} u_g \end{aligned} \tag{4}$$

$$\begin{aligned} i_{2oD}(s) = {} & \frac{G_D K_{\text{PWM}} G_i}{L_1\,(L_2+L_g)\,Cs^3 + C(L_2+L_g)KG_D K_{\text{PWM}}s^2 + (L_1+L_2+L_g)\,s + KG_D K_{\text{PWM}}} \times i_{2\text{ref}} \\ & - \frac{s^2 L_1 C + sCG_D K_{\text{PWM}}K + 1}{s^3 L_1\,(L_2+L_g)\,C + C(L_2+L_g)KG_D K_{\text{PWM}}s^2 + s\,(L_1+L_2+L_g) + KG_D K_{\text{PWM}} + K_{\text{PWM}}G_D G_i} \times u_g \end{aligned} \tag{6}$$

$$\begin{aligned} i_{2cD}(s) = {} & \\ & \frac{(K_P K_{\text{PWM}} s + K_I K_{\text{PWM}})\,G_D}{L_1\,(L_2+L_g)\,Cs^4 + C(L_2+L_g)KG_D K_{\text{PWM}}s^3 + (L_1+L_2+L_g)\,s^2 + (K_P+K)\,G_D K_{\text{PWM}}s + K_I G_D K_{\text{PWM}}} i_{2\text{ref}} \\ & - \frac{L_1 Cs^3 + CKK_{\text{PWM}}G_D s^2 + s}{L_1\,(L_2+L_g)\,Cs^4 + C(L_2+L_g)KK_{\text{PWM}}G_D s^3 + (L_1+L_2+L_g)\,s^2 + (K_P+K)\,K_{\text{PWM}}G_D s + K_I K_{\text{PWM}}G_D} u_g \\ = {} & i_{2\_iD} + \Delta i_{2\_gD} \end{aligned} \tag{7}$$

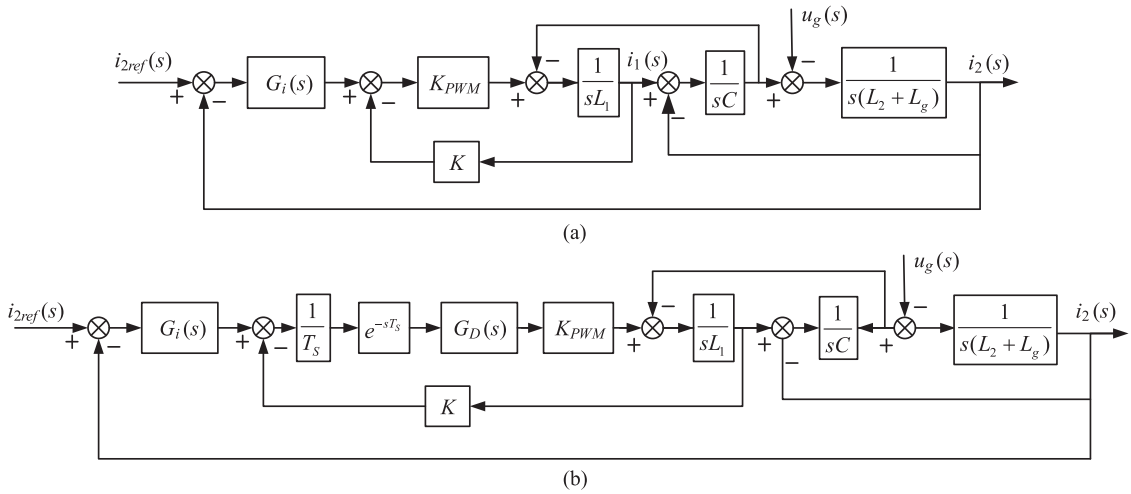

Fig. 2. Equivalent block diagram of GCI-*LCL* under the proposed dual-current control strategy. (a) Without time delay. (b) With time delay.

TABLE I
ROUTH ARRAY OF THE GRID-CONNECTED INVERTER WITH *LCL* FILTER UNDER THE DUAL-CURRENT CONTROL STRATEGY

s^5:	$1.5L_1(L_2+L_g)CT_S$	$(L_2+L_g)CKK_{PWM}+1.5(L_1+L_2+L_g)T_S$	$(K_P+K)K_{PWM}$
s^4:	$L_1(L_2+L_g)C$	$L_1+L_2+L_g$	K_IK_{PWM}
s^3:	$(L_2+L_g)CKK_{PWM}$	$(K+K_P)K_{PWM}-1.5T_SK_IK_{PWM}$	
s^2:	$\left(L_1+L_2+L_g\right)-\frac{\left(K+K_P-1.5T_SK_I\right)L_1}{K}$	K_IK_{PWM}	
s^1:	R_{S1}		
s^0:	K_IK_{PWM}		

Note: $R_{S1}=(K+K_P)K_{PWM}-1.5T_SK_IK_{PWM}-\frac{(L_2+L_g)CKK_{PWM}^2K_I}{(L_1+L_2+L_g)K-(K+K_P-1.5T_SK_I)L_1}$.

III. SYSTEMATIC PARAMETERS DESIGN PROCESS OF THE PROPOSED CONTROL STRATEGY

In the proposed dual-current feedback control strategy, the inverter-side current feedback parameter K and the PI controller parameters K_P and K_I have significant influences on GCI-*LCL* performance, including the resonance frequency, resonance suppression, stability margin, and grid-connected characteristics. To satisfy the above-mentioned requirements, the systematic parameters design process is presented as follows.

1) Stability limitation of parameters considering time delay.
2) Resonance suppression of the *LCL* filter provided by the inverter-side current feedback to determine parameter K.
3) Proposing a simplified model in a low-frequency band.
4) Design of PI controller parameters with a hybrid model considering grid-connected demands and system stability.

A. Parameters Stability Limitation With Time Delay Based on the Routh–Hurwitz Criterion

According to one-order Taylor expansion, the time delay model G_D can be rewritten as

$$G_D(s)=\frac{1}{1+1.5T_Ss}. \tag{9}$$

According to (6)–(9), the characteristic equation of the close-loop system is

$$\begin{aligned}D_{cD}(s)&=1.5L_1(L_2+L_g)CT_Ss^5+L_1(L_2+L_g)Cs^4\\&+\left[(L_2+L_g)CKK_{PWM}+1.5\left(L_1+L_2+L_g\right)T_S\right]s^3\\&+\left(L_1+L_2+L_g\right)s^2+\left(K+K_P\right)K_{PWM}s+K_IK_{PWM}.\end{aligned} \tag{10}$$

From (10), the Routh array of GCI-*LCL* under the proposed strategy is shown in Table I. According to the Routh–Hurwitz criterion, if the poles of the system are not in the right half-plane, the elements in the first column of the Routh array and the elements in the characteristic equation of the close-loop system should be equal to or greater than zero. Thus, to ensure the stability of GCI-*LCL*, the parameter ranges of K, K_P, and K_I are

$$\begin{cases}K>\dfrac{L_1}{L_2+L_g}\left(K_P-1.5T_SK_I\right)\\K+K_P>1.5T_SK_I>\dfrac{L_1}{L_2+L_g}\left(K_P-K\right)\\\dfrac{L_2+L_g}{L_1}K+1.5T_SK_I>K_P>1.5T_SK_I-K\\R_{S1}>0.\end{cases} \tag{11}$$

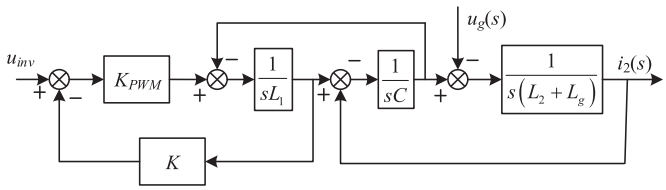

Fig. 3. Control block diagram of the inverter-side current feedback.

From (11), with the increase of grid inductance L_g, the value ranges of K, K_P, and K_I to ensure the stability of GCI-*LCL* increase.

B. Inverter-Side Current Feedback Designed and the Simplified System Model in a Low-Frequency Band

The control block diagram of GCI-*LCL* with inverter-side current feedback is shown in Fig. 3. According to the figure, the characteristic equation is expressed as

$$D_o(s) = as^3 + bs^2 + cs + d = 0 \tag{12}$$

where $a = L_1(L_2 + L_g)C, b = C(L_2 + L_g)KK_{\mathrm{PWM}}, c = L_1 + L_2 + L_g, d = KK_{\mathrm{PWM}}$. Comparing with (1), $D_o(s)$ adds the damping terms $CL_2KK_{\mathrm{PWM}}s^2$ and KK_{PWM}.

From (12), the characteristic equation of GCI-*LCL* with inverter-side current feedback is a general three-order function. According to Cardano's method, if K is larger than zero, the discriminant Δ will be greaters than zero

$$\begin{aligned}\Delta &= (ba - 9ad)^2 - 4\left(b^2 - 3ac\right)\left(c^2 - 3bd\right) \\ &= 3L_2^6\begin{bmatrix} e^2K^2K_{\mathrm{PWM}}^2\left(27y^3 + 26y^2 - 2y - 1\right) \\ +4(1+y)^3ye + 4e^3K^4K_{\mathrm{PWM}}^4 \end{bmatrix} > 0.\end{aligned} \tag{13}$$

Thus, the equation has one real root and two conjugate complex roots, and the system characteristic function with inverter-side current feedback can be rewritten as

$$D_o(s) = (ms + n)\left(s^2 + \xi\omega_{\mathrm{inv}}s + \omega_{\mathrm{inv}}^2\right) = 0 \tag{14}$$

where $-n/m, \xi$, and ω_{inv} are the real root, damping ratio, and resonance frequency of GCI-*LCL* with inverter-side current feedback

$$\begin{cases} \xi = \dfrac{-b + \frac{1}{2}\left(\sqrt[3]{Y_1} + \sqrt[3]{Y_2}\right)}{3a \cdot \omega_{\mathrm{inv}}} \\ \omega_{inv} = \dfrac{1}{3a}\sqrt{\left[-b + \dfrac{1}{2}\left(\sqrt[3]{Y_1} + \sqrt[3]{Y_2}\right)\right]^2 + \dfrac{3}{4}\left(\sqrt[3]{Y_1} + \sqrt[3]{Y_2}\right)^2} \\ -\dfrac{n}{m} = \dfrac{-b - \dfrac{1}{2}\left(\sqrt[3]{Y_1} + \sqrt[3]{Y_2}\right)}{3a} \end{cases} \tag{15}$$

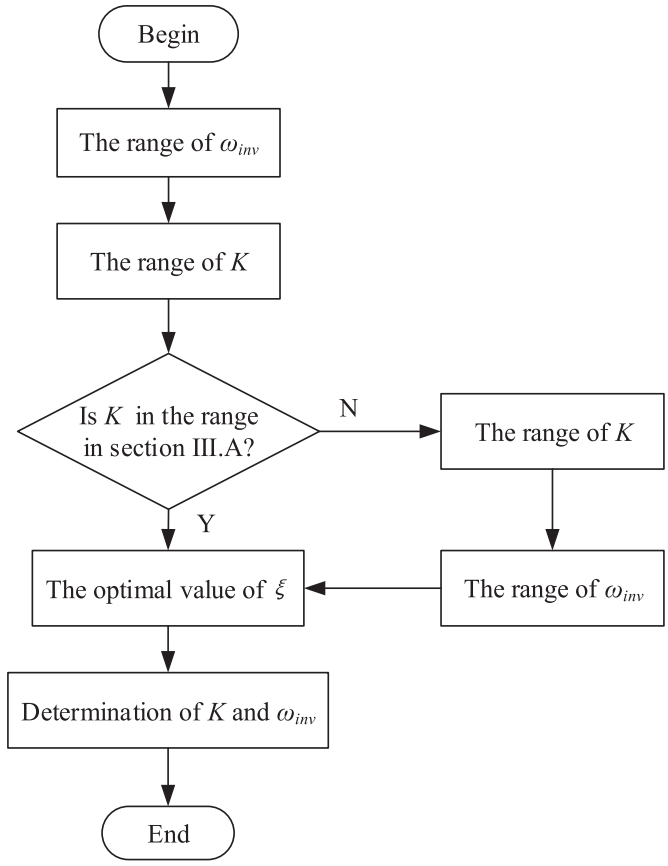

Fig. 4. Design process of parameter K in the inverter-side current feedback loop.

$$\begin{cases} e = C/(L_2 + L_g), y = L_1/(L_2 + L_g) \\ Y_{1,2} = e^2L_2^6KK_{\mathrm{PWM}}\left[K^2K_{\mathrm{PWM}}^2 - 3ey(1+y)\right] \\ \quad +\frac{3}{2}eyL_2^3\left[eL_2^3KK_{\mathrm{PWM}}\left(8y - 1\right) \pm \sqrt{\Delta}\right]. \end{cases} \tag{16}$$

However, the resonance frequency of GCI-*LCL* with an active damping method is often ignored. If the resonance frequency is between 10 f_n and 1/4 f_S, the better dynamic response and harmonic current suppression can be achieved [31]. According to (15), the damping ratio ξ, the inverter-side current feedback parameter K, and the resonance frequency ω_{inv} are interconnected. Besides, K must be in the stability limitation in (11).

The design process of ξ, K, and ω_{inv} is depicted in Fig. 4. First, the range of resonance frequency in GCI-*LCL* can be determined by switch frequency. The range of K can be determined according to (15) subsequently. If the range of K is in the stability limitation in (11), the optimal value of ξ is achieved at the next step. If not, the ranges of K and ω_{inv} must be modified to enter the stability limitation in (11). Then, the optimal value of ξ is allowed to be determined. Finally, K and ω_{inv} are determined.

Then, the Bode diagram of GCI-*LCL* with inverter-side current feedback is shown in Fig. 5. From the figure, the inverter-side current feedback can provide damping for the resonance of

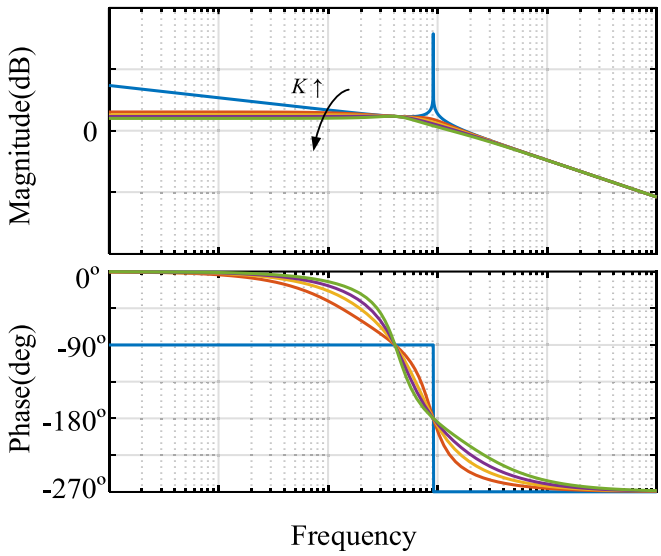

Fig. 5. Bode diagram of GCI-*LCL* with the inverter-side current feedback.

the *LCL* filter. When K varies, the damping ratio ξ is a maximum value. Moreover, the cross frequency ω_c of the system is smaller than the resonance frequency ω_{inv} with inverter-side current feedback. On the other hand, the two conjugate complex roots of the characteristic equation of GCI-*LCL* with inverter-side current feedback are far from the imaginary axis. Thus, to simplify the systematic design process of control system parameters, the simplified system transfer function in the low-frequency band is proposed

$$G_{\text{inv}} = \frac{1}{K}. \tag{17}$$

According to (17), the phase–frequency curve begins at zero, and the magnitude–frequency curve is paralleled with the frequency axis. It matches the curves in the low-frequency band in the Bode diagram of GCI-*LCL* presented in Fig. 5. Hence, in the low-frequency band or fundamental frequency, the simplified model is correct and feasible, and the influence of the weak grid on the GCI-*LCL* is reduced obviously.

C. Design of the PI Controller

PI controller parameters have a strong influence on the robustness and stability of GCI-*LCL*. Since the corner frequency ω_i is suggested to be set lower than ω_{inv}, $G_i(s)$ can be approximated to K_P at the frequencies higher than ω_{inv} [32]. In this section, the PI controller parameters are determined by the stability margin, interference suppression of grid voltage, and dynamic response.

According to (15) and Fig. 4, the resonance frequency of GCI-*LCL* can be determined. In the Bode diagram of the system open-loop transfer function, the phase-frequency curve crosses the –180° at the resonance frequency of the *LCL* filter. Thus, in the GM design, the model of GCI-*LCL* with inverter-side current feedback is considered, and the system GM can be depicted as

$$-20\lg\left|\left(K_P+\frac{K_I}{s}\right)\cdot\frac{K_{\text{PWM}}}{\begin{array}{l}L_1(L_2+L_g)Cs^3+CL_2KK_{\text{PWM}}s^2\\+(L_1+L_2+L_g)s+KK_{\text{PWM}}\end{array}}\right|_{s=j\omega_{\text{inv}}}\geq \text{GM}. \tag{18}$$

Considering the grid inductance L_g, the range of K_P increases. Hence, the range of K_P without grid inductance L_g is

$$K_P \geq \frac{\left|\begin{array}{l}L_1L_2Cs^3+CL_2KK_{\text{PWM}}s^2\\+(L_1+L_2)s+KK_{\text{PWM}}\end{array}\right|_{s=j2\pi f_{LCL}}}{K_{\text{PWM}}\times 10^{\frac{\text{GM}}{20}}}. \tag{19}$$

From (19), if C or L_1 increases, the range of K_P decreases. The cross frequency ω_c of GCI-*LCL* is much smaller than the resonance frequency of the *LCL* filter, even after damping. Thus, the system transfer function with the PI controller at the low-frequency band is

$$G_{\text{op}} = G_i\cdot G_{\text{inv}} = \left(K_P+\frac{K_I}{s}\right)\cdot\frac{1}{K}. \tag{20}$$

Then, the PM of the system can be described as

$$180^\circ+\angle\frac{(K_Ps+K_I)}{s\cdot K}\geq \text{PM}. \tag{21}$$

Generally, the PM value should be greater than 45° to ensure the stability of the system under disturbance. Considering the cross frequency of the system as (22), the ranges of K_P and K_I can be obtained as (23) and (24), respectively,

$$\omega_c = \frac{K_I}{\sqrt{K^2-K_P^2}} \leq 10f_n\times 2\pi \tag{22}$$

$$0<K_P\leq K \tag{23}$$

$$K_I \leq 10f_n\times 2\pi\times\sqrt{K^2-K_P^2}. \tag{24}$$

In this paper, the GCI-*LCL* operates in unity PF. Thus, the ideal grid-connected current i_{2_iD} coincides with the grid voltage u_g in the ABC coordinate. Besides, the inference current of grid voltage Δi_{2_gD} lags behind u_g with 90°. Considering the grid-connected current i_{2_iD} and the inference current of grid voltage Δi_{2_gD}, the output power-factor angle can be defined as

$$\tan\delta = \frac{\Delta i_{2\_gD}}{i_{2\_iD}} = \frac{(L_1Cs^3+CKG_DK_{\text{PWM}}s^2+s)u_g}{G_DK_{\text{PWM}}(K_Ps+K_I)i_{2\text{ref}}}. \tag{25}$$

Because the rated frequency of grid voltage is much smaller than the cross frequency of GCI-*LCL*, K_P and G_D can be ignored at the fundamental frequency [27]. When the output PF

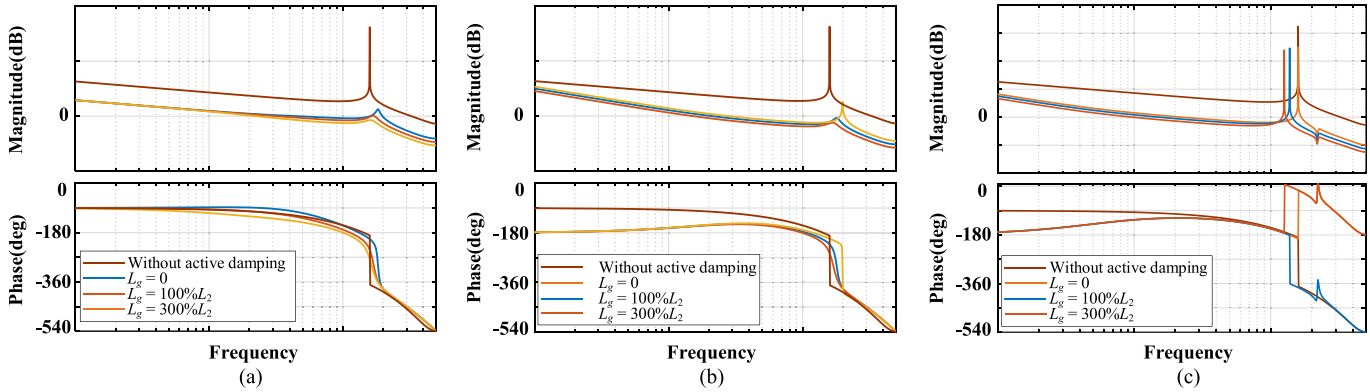

Fig. 6. Bode diagrams of GCI-*LCL* interfered by the weak grid. (a) Under the proposed strategy. (b) Under the conventional active damping control strategy based on capacitor current and grid-connected current feedback. (c) Under the additional filter strategy based on the notch filter.

$\cos\delta$ is achieved, K_I is limited as

$$\tan\delta = \frac{\Delta i_{2\_g}}{i_{2\_i}} = \frac{(L_1Cs^3 + CKK_{\mathrm{PWM}}s^2 + s)u_S}{(K_PK_{\mathrm{PWM}}s + K_IK_{\mathrm{PWM}})i_{2\_\mathrm{ref}}}\bigg|_{s=j2\pi f_n} \leq \frac{\sqrt{1-\cos^2\delta}}{\cos\delta}\bigg|_{\cos\theta=0.9} \Leftrightarrow K_I \geq \frac{(L_1Cs^3 + CKK_{\mathrm{PWM}}s^2 + s)u_g}{\tan\delta \times K_{\mathrm{PWM}} \times i_{2\mathrm{ref}}}. \quad (26)$$

D. Comparison Between the Proposed Strategy and the Conventional Control Strategy

The bode diagrams of GCI-*LCL* with the proposed strategy, the conventional active damping strategy based on capacitor current and grid-connected current feedback, and the additional filter strategy based on the notch filter are depicted in Fig. 6. In damping characteristic, the proposed strategy and the conventional active damping strategy both have ideal resonance suppression effect of GCI-*LCL* considering time delay, which is better than that under the additional filter strategy. Besides, in anti-interference capability, when the *LCL* filter is disturbed by increased grid impedance, the proposed strategy maintains a steady state at the low-frequency band. In contrast, the gains and system cross frequencies under the conventional active damping strategy and additional filter strategy are decreased. It has a significant influence on the output characteristics of GCI-*LCL*, such as PF and THD of the grid-connected current. Moreover, in the stability margin of the system, the proposed strategy maintains a larger stability margin than the conventional active damping strategy and additional filter strategy, even if the *LCL* filter is disturbed by the weak grid.

IV. Case Study

A design example for GCI-*LCL* under the proposed strategy is discussed in this section. The main parameters of GCI-*LCL* are shown in Table II. According to the *LCL* filter design criteria, the *LCL* filter for a 3 kW GCI-*LCL* prototype is set up and satisfies the requirements as follows.

1) THD of the grid-connected current is less than 5%.

TABLE II
Basic Parameters of the Grid-Connected Inverter With *LCL* Filter

Parameter	Value
L_1	1.5 mH
L_2	1.5 mH
C	10 μF
U_{dc}	360 V
u_g	220 V
f_n	50 Hz
f_S	10 kHz
P_n	3 kW

2) PF is larger than 0.9.
3) Inverter-side current ripple is less than 20%.
4) Reactive power caused by the capacitor is less than 10%.
5) Switching harmonics is less than 3%.
6) Resonance frequency is between $10f_n$ and $0.5f_s$.

From (11), K, K_P, and K_I are larger than zero, and their ranges can be calculated by the Routh–Hurwitz criterion as

$$K + K_P > 1.5T_SK_I > K_P - K \quad (27)$$

$$(K + K_P) - 1.5T_SK_I - \frac{CKK_{\mathrm{PWM}}K_I}{K - (K_P - 1.5T_SK_I)} > 0. \quad (28)$$

Then, to achieve the resonance suppression for the *LCL* filter, K is determined. According to (15), the range of $\omega_{\mathrm{inv}}, \xi$ gains the maximum of 0.27, if K and ω_{inv} are determined as 0.057 and 9726 rad/s, respectively. To satisfy the requirements of PM $>$ 40°, GM $>$ 3 dB, and PF $>$ 0.9 at rated power P_n, the region of K_P and K_I is calculated according to (19), (23), (24), and (26)–(28), as shown in Fig. 7. Moreover, considering the variation of L_1 ($\pm$20%), L_2 (0 $-$ 400%), and C ($\pm$20%), the range of K_P is decreased from [0.0335, 0.057] to [0.0418, 0.057] according to (27). Thus, K_P is set as 0.05. To achieve a better PF (PF $>$ 0.98), the range of K_I is decreased from [60, 100] to [70, 100] at $K_P = 0.05$. Then, $K_P = 0.05$ and $K_I = 90$ at point A are set to achieve a larger stability margin. The fundamental frequency gain ($\omega_{\mathrm{inv}} = 100\,\pi$rad/s) is 14 dB. Besides, the PM and GMs

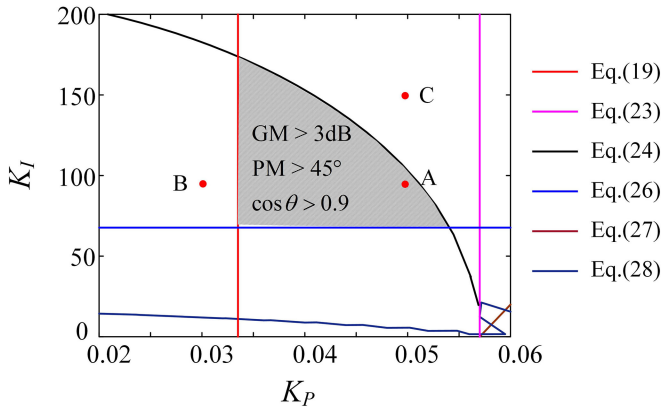

Fig. 7. Range of the parameters in the PI controller with multirestrictions.

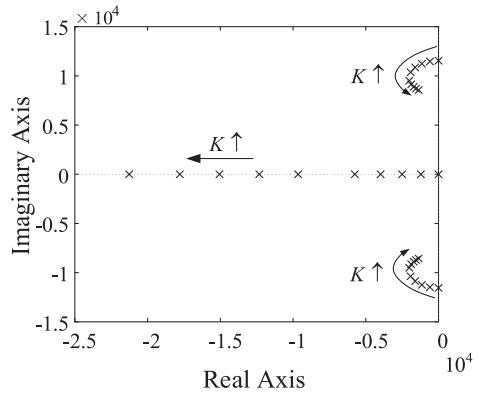

Fig. 8. Root locus of the open-loop system before the compensation of the PI controller.

are 89.2°, 3.71 dB, and –6.57 dB, respectively, thus satisfying the stability requirement and the anti-interference of the system. However, point B ($K_P = 0.03, K_I = 90$) is out of the region, and the PM and GMs are 92.1°, 8.14 dB, and 0.10 dB, and point C ($K_P = 0.05, K_I = 150$) is also out of the region, and the PM and GMs are 41.8°, 2.0 dB, and –7.8 dB, as shown in Fig. 7. From the figure, the PMs of points A and B vary slightly around 90°, which are larger than the PM of point C. However, the GMs of point B are larger than zero, and the corresponding system is unstable. The GM of point C is less than 3 dB of point A, and the corresponding system is stable. Therefore, the point at the shadow area, which is the overlapping area of (23)–(28), ensures the stable operation of the system and satisfies the grid-connected requirements, and the points out of the shadow area lead to dissatisfaction of part or all of the requirements for GCI-*LCL* stable operation.

The pole-zero map of the open-loop system before the compensation of the PI controller with the increase of K is presented in Fig. 8. As can be seen from the figure, a pair of conjugate poles get away from the imaginary axis and then close to the imaginary axis with the increase of K. Hence, the damping ratio would reach the maximum value, and the resonance frequency would be decreased with the increase of K. Moreover, the real pole gets away from the imaginary axis quickly with the increase of K. Thus, the equivalent model at the low-frequency band is a proportional model, and K affects the equivalent model at the low-frequency band, the resonance frequency, and the damping ratio significantly.

To verify the stability and anti-interference capability of the system, the model with time delay is established, and the time delay equals to the sample time (100 μs). The bode diagrams of GCI-*LCL* interfered by *LCL* parameters, and the weak grid under the proposed strategy are presented in Fig. 9. When the inverter-side inductance L_1 in the *LCL* filter is disturbed and varies from 12 to 18 mH ($\pm 20\%$), the Bode diagram of the open loop in GCI-*LCL* is shown in Fig. 9(a). From the figure, with the variation of L_1, the fundamental frequency gain is almost undisturbed at 14 dB, the GMs vary from 4.5 to 3.31 dB and from –3.2 to –42.5 dB, and the PM varies from 89.2° to 66.2°. Thus, the system still operates with high stability. When the capacitor C in the *LCL* filter is disturbed and varies from 8 to 12 μF ($\pm 20\%$), the Bode diagram of the open loop in GCI-*LCL* is shown in Fig. 9(b). From the figure, with the variation of C, the fundamental frequency gain is almost undisturbed at 14 dB, the GMs vary from 3.77 to 2.66 dB and from –3.67 to –13.7 dB, and the PM decreases from 84.4° to 58.4°. Thus, the system still operates with high stability. With the selected grid inductance $L_g = 0, 1.6$, and 4.8 mH, the Bode diagram of the open loop in GCI-*LCL* interfered by grid inductance L_g is shown in Fig. 9(c). From the figure, with the variation of L_g, the fundamental frequency gain is almost undisturbed at 14 dB, the GMs vary from 3.31 to 12.3 dB and –6.57 to –13 dB, and the PM decreases from 79.2° to 67.8°. Thus, the resonant angular frequency decreases to the frequency near or less than the cross angular frequency of the PI controller, and it has an adverse impact on the PM of the system. According to the analysis, with the interference from *LCL* parameters and weak grid, the GCI-*LCL* operates in a high stable state under the proposed control strategy.

The bode diagrams of GCI-*LCL* interfered by the weak grid under the conventional active damping strategy and additional filter strategy are shown in Fig. 9(d) and (e). Their equivalent inductance at the low-frequency band is a single inductor filter ($L_1 + L_2 + L_g$), which is affected by the grid impedance. With the increased disturbance of L_g, under the conventional active damping strategy based on capacitor current and grid-connected current feedback, the fundamental frequency gain changes from 32.8 to 24.8 dB, the GM varies from 5.66 to 11.8 dB, and the PM varies slightly from 33.8° to 31.3°. With the selected grid inductance $L_g = 0, 1.6$, and 4.8 mH, under the additional filter strategy based on a notch filter, the fundamental frequency gains are 18.5, 14.9, and 10.5 dB, the GMs are 3.47, 6.12, and 7.19 dB, and the PMs are 59.1°, 62.4°, and 60.9°, respectively. Therefore, with the increase of L_g, the fundamental frequency gain under conventional active damping strategy and additional filter strategy is varied, bringing instability to the system. Besides, the GM and PM under the conventional active damping strategy and additional filter strategy are both smaller than that under the proposed control strategy.

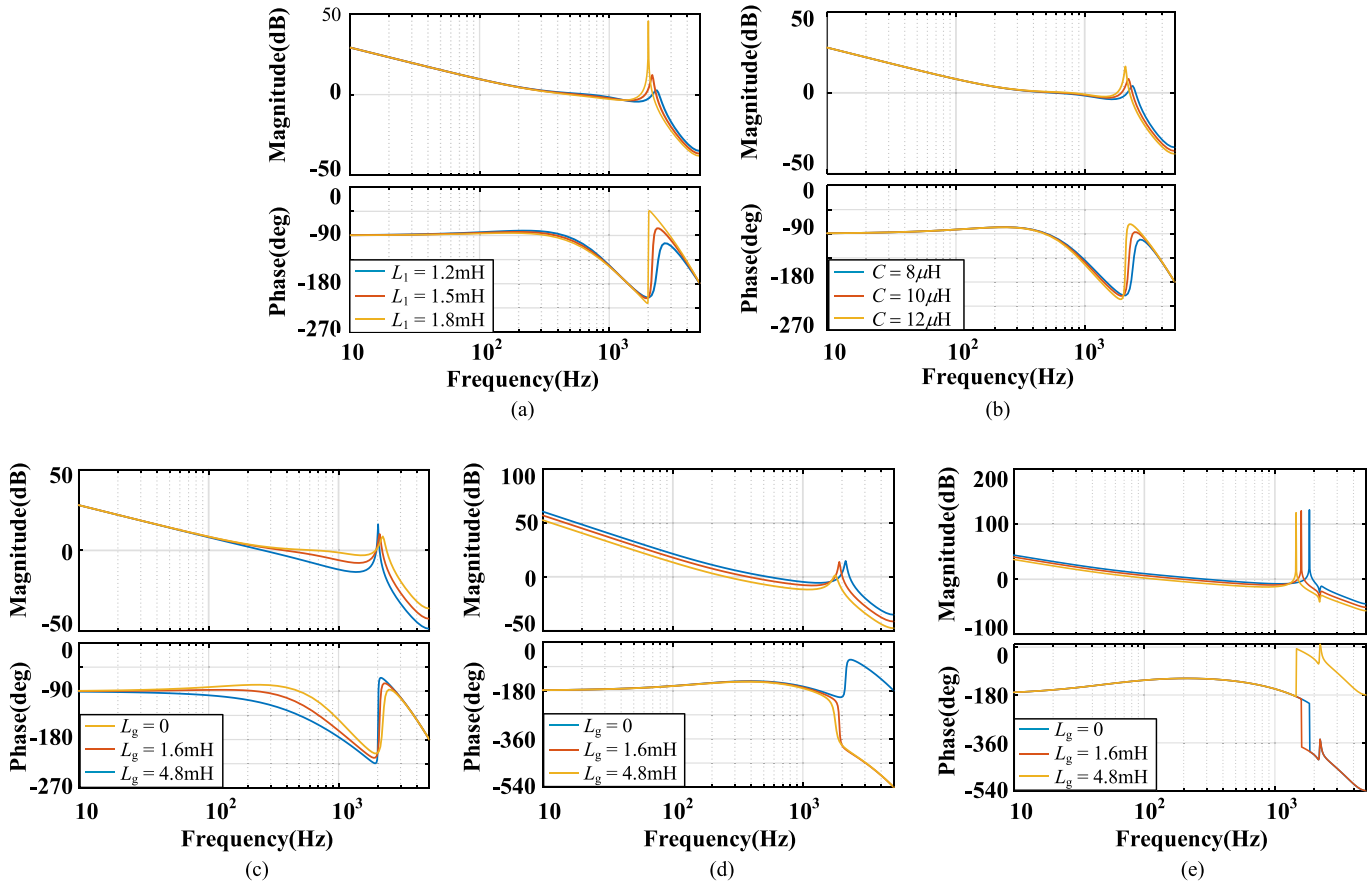

Fig. 9. Bode diagrams of GCI-*LCL* interfered by *LCL* parameters and the weak grid. (a) L_1 disturbance under the proposed strategy. (b) C disturbance under the proposed strategy. (c) With the weak grid under the proposed strategy. (d) With the weak grid under the conventional active damping strategy based on capacitor current and grid-connected current feedback. (e) With the weak grid under the additional filter strategy based on the notch filter.

From the case study mentioned above, compared with the conventional active damping control strategies, the proposed strategy has a larger stability margin, a higher anti-interference capability, and a more stable gain at the low-frequency band. Moreover, compared with the additional filter strategy, the proposed strategy has a better resonance suppression effect with time delay. Under the proposed control strategy, the equivalent effect on the low-frequency band with inverter-side current feedback is only related to the parameter K, which obtains a higher anti-interference capability and a better filtering performance with the variation of parameters, especially with the grid impedance in the weak grid. Moreover, the grid-current feedback is used as an outer loop of current control, so that the design process of the controller is more concise and clear. Therefore, the proposed control strategy has a better anti-interference performance and can be adopted in the application with disturbance from circuit parameters and weak grid.

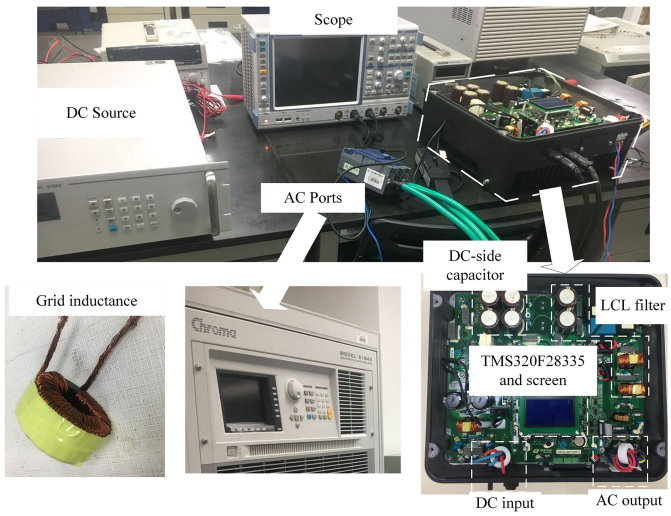

Fig. 10. GCI-*LCL* prototype and experiment setup.

V. Verification in Experiments

To verify the correctness and effectiveness of the analysis and the proposed strategy, a 3 kW GCI-*LCL* prototype is set up, as shown in Fig. 10. The main circuit parameters of the GCI-*LCL* prototype are presented in Table II, and the controller parameters are discussed in Section IV. The experiment setup is composed of:

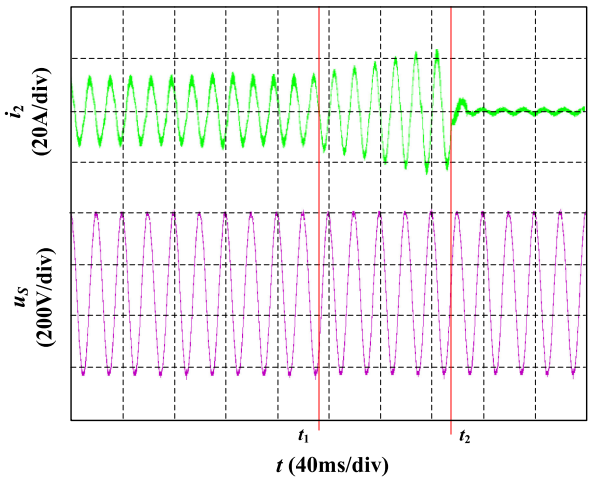

Fig. 11. Experiment results under the proposed control strategy, when inverter-side current feedback parameter K changes from 0.057 to 0.

1) a programmable ac source (Chroma 61845) with the grid impedance;
2) the GCI-*LCL* prototype with a TMS320F28335 DSP controller;
3) a programmable dc source (Chroma 61604);
4) a scope for currents and voltages measurement.

A. Experiment Results When $L_g = 0$

When the inverter-side current feedback parameter K changes from 0.057 to 0 with $L_g = 0$, the experiment results under the proposed strategy are shown in Fig. 11. Before the time t_1, the GCI-*LCL* operates steadily with full load under the proposed strategy. At time t_1, the parameter K suddenly changes from 0.057 to 0, the GCI-*LCL* changes from stable state to divergent state subsequently, and the grid-connected current i_2 increases rapidly. At the time t_2, the grid-connected current exceeds the overload current, and the GCI-*LCL* is out of operation. Thus, under the proposed strategy with the active damping $K = 0.057$, the GCI-*LCL* works steadily. However, when the active damping $K = 0$, the grid-connected current is divergent, thus leading to an unstable case and off-grid operation.

The grid voltage and grid-connected current with $L_g = 0$ are shown in Fig. 12(a). As can be seen from the figure, the grid voltage at PCC u_g is stable without harmonic distortion. Besides, the THD in grid-connected current i_2 is 3.02% and the PF is 99.3%, satisfying the operation requirement of the grid-connected current in the grid. The inverter-side currents under the proposed strategy and the conventional active damping strategy based on capacitor current and grid-connected current feedback are shown in Fig. 12(b). As can be seen from the figure, the THD of inverter-side current i_1 under the conventional active damping strategy is 7.74%. On the other hand, the THD of the inverter-side current under the proposed strategy is 4.53%. Therefore, the GCI-*LCL* under the proposed control strategy obtains lower THD of the inverter-side current than that under the conventional active damping strategy, satisfying the operation requirement of the inverter-side current in the power grid and protecting the switches in bridge arms.

B. Experiment Results With Grid Inductance

When the GCI-*LCL* operates in the weak grid $L_g = 1.6$ mH, the experiment results under the proposed control strategy, the conventional active damping strategy based on capacitor current and grid-connected current feedback, and the additional filter strategy based on the notch filter are shown in Fig. 13. From the figure, the THD of grid-connected current i_2 under the proposed control strategy is 3.13%, which is lower than 3.47% under the conventional active damping strategy and 4.14% under the additional filter strategy. Besides, the PF under the proposed control strategy is 99.2%, which is higher than 97.2% under the conventional active damping strategy and 95.9% under the additional filter strategy. Moreover, the load change happens at t_a, t_b, and t_c in Fig. 13(a), (b), and (c), respectively. In Fig. 13(a), the grid-connected current i_2 under the proposed control strategy has no overshoot, and the dynamic response adjust time is about 3.8 ms. In Fig. 13(b), the grid-connected current i_2 under the conventional active damping strategy also has no overshoot, and the dynamic response adjust time is about 4 ms. In Fig. 13(c), the grid-connected current i_2 under the additional filter has an overshoot of about 8.5 A, and the dynamic response adjust time is about 5.7 ms. According to the experiment results, the GCI-*LCL* under the proposed control strategy obtains lower THD of the grid-connected current, higher PF and no overshoot, and better dynamic response characteristics during load change occasion.

When GCI-*LCL* operates with $L_g = 4.8$ mH, the experiment results under the proposed control strategy and the conventional active damping strategy based on capacitor current and grid-connected current feedback, and the additional filter strategy based on the notch filter are shown in Fig. 14. The THDs of grid-connected current i_2 are 3.24%, 4.05%, and 5.75% in Fig. 14(a), (b), and (c), respectively. Thus, the GCI-*LCL* under the proposed control strategy obtains a better damping effect than the conventional active damping strategy and additional filter strategy. Besides, the PF is 99.0%, 95.6%, and 94.3% in Fig. 14(a), (b), and (c), respectively. Thus, the GCI-*LCL* under the proposed control strategy obtains larger stable gain at the fundamental frequency than the conventional active damping strategy and additional filter strategy. Moreover, the overshoots of grid-connected current i_2 are 7.3, 8.2, and 16.6 A, and the dynamic response adjust time is 5.1, 3.2, and 6.1 ms in Fig. 14(a), (b), and (c), respectively. Thus, the GCI-*LCL* under the proposed control strategy obtains lower overshoot and better dynamic response characteristics during the load change occasion. In addition, the dynamic response adjustment time becomes larger with the increase of grid inductance.

The comparison of PFs under the proposed control strategy and the conventional damping control strategies in the weak grid is shown in Fig. 15(a). The GCI-*LCL* operates in full load, and the grid inductance increases with 0, 0.3, 0.8, 1.6, 3.2, 4.8, 6.4, and 8 mH. Under the proposed control strategy, the

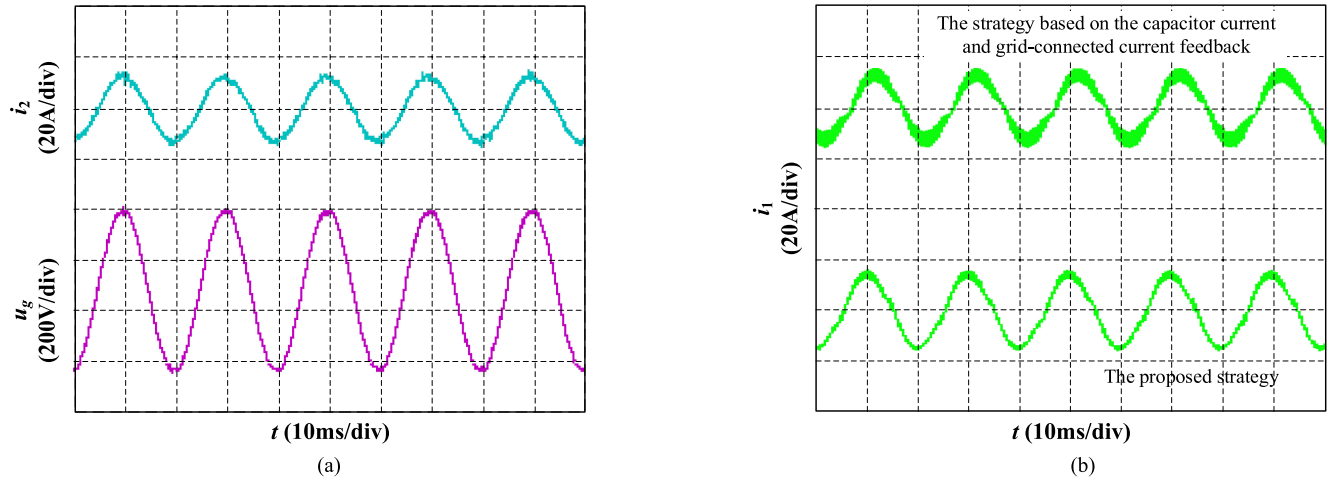

Fig. 12. Steady experiment results. (a) Voltage at PCC u_g and the grid-connected current i_2. (b) Comparison of inverter-side current i_1 under the proposed strategy and the conventional active damping strategy based on capacitor current and grid-connected current feedback.

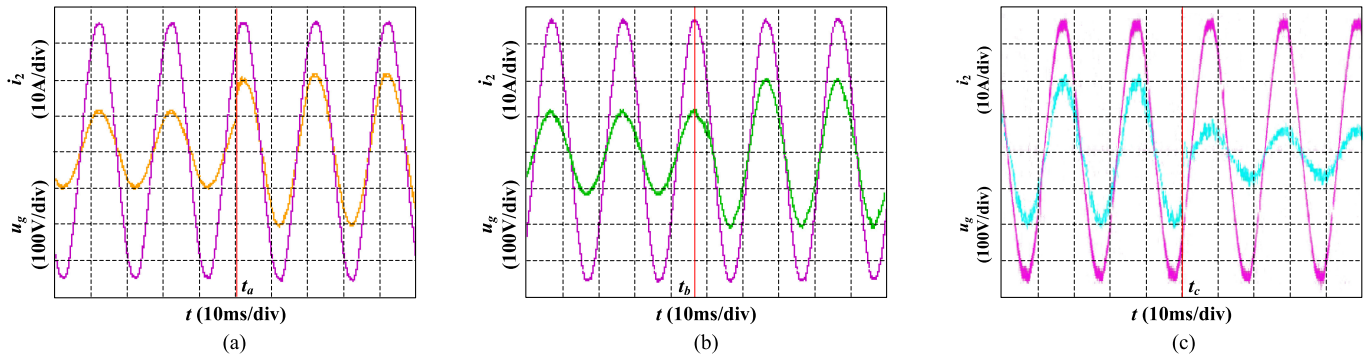

Fig. 13. Grid voltage at PCC and grid-connected current with $L_g = 1.6$ mH. (a) Under the proposed control strategy. (b) Under the conventional active damping strategy based on capacitor current and grid-connected current feedback. (c) Under the additional filter strategy based on the notch filter.

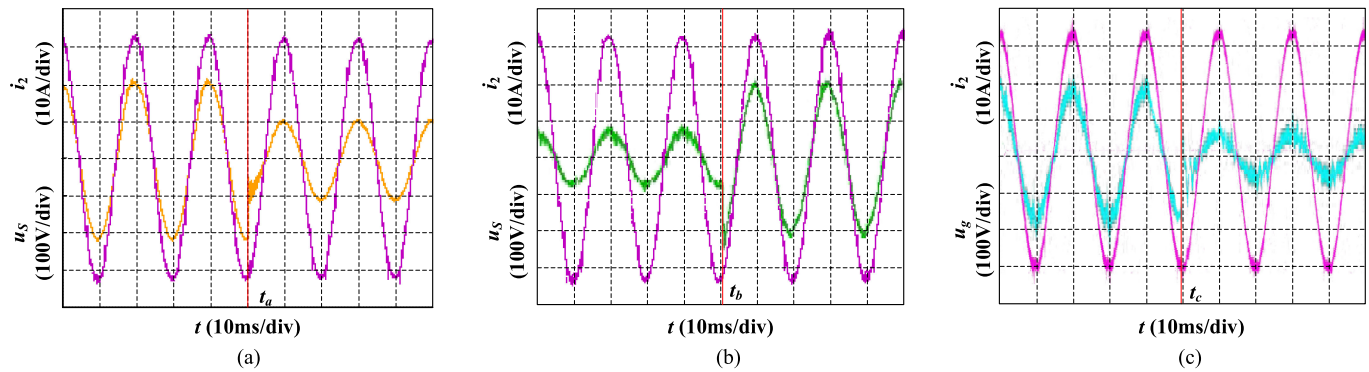

Fig. 14. Grid voltage at PCC and grid-connected current with $L_g = 4.8$ mH. (a) Under the proposed control strategy. (b) Under the conventional active damping strategy based on capacitor current and grid-connected current feedback. (c) Under the additional filter strategy based on the notch filter.

PF maintains a steady state about 99% with the disturbance of the weak grid. On the other hand, the PFs decrease from 99.4% to 93.8% under the conventional active damping strategy and from 98.9% to 93.2% under the additional filter strategy. Then, the comparison of THDs of grid-connected current i_2 under the proposed control strategy and the conventional control strategies in the weak grid is shown in Fig. 15(b). When the grid inductance increases, the THDs of grid-connected current i_2 under the proposed control strategy and conventional control strategies all increase. However, the THD of grid-connected current i_2 under the proposed control strategy has the minimum increase, maintaining the lowest THD value.

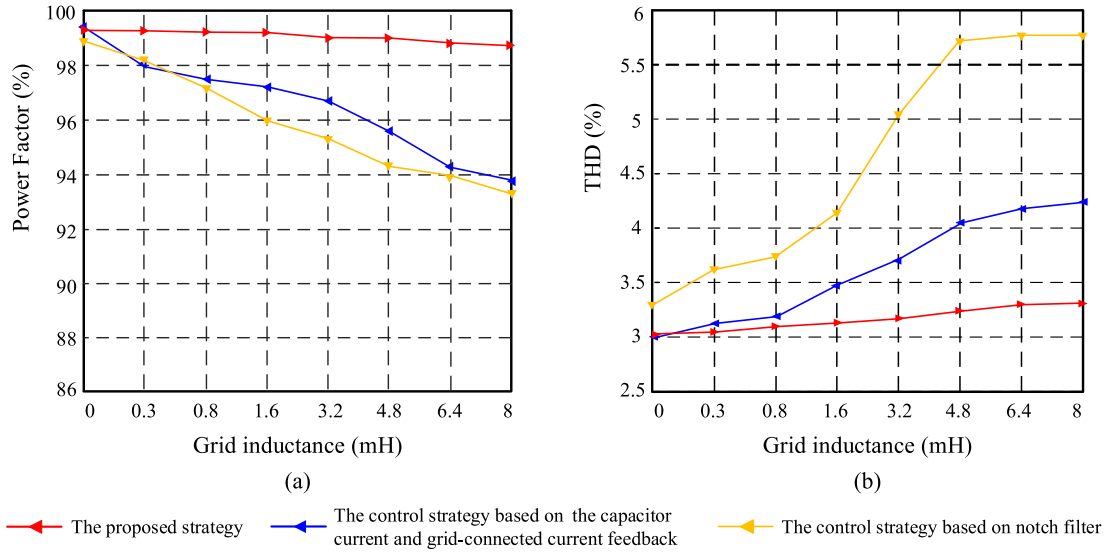

Fig. 15. Comparison of power factor and THD of grid-connected current i_2 under the proposed control strategy and the control conventional active damping strategy and the additional filter strategy in the weak grid.

VI. Conclusion

To achieve the resonance suppression of the *LCL* filter, a larger stability margin, the robustness of GCI-*LCL*, and better grid-connected characteristics in the weak grid, a dual-current feedback active damping control strategy based on inverter-side current and grid-connected current feedback is proposed in this paper. Then, the active damping characteristic of GCI-*LCL* based on the inverter-side current feedback is analyzed, and the Routh–Hurwitz criterion, stability margin, output PF, and active damping characteristic of the system are investigated to achieve the ranges of parameters. Moreover, the systematic parameters design process is discussed and verified by the root locus diagram and Bode diagram in a case study. A 3 kW GCI-*LCL* prototype is set up and the experiments are conducted. The experiment results verify the correctness and feasibility of the analysis and proposed strategy. Comparing with the conventional active damping strategy and the additional filter strategy, GCI-*LCL* under the proposed dual-current feedback control strategy achieves an ideal resonance suppression, a larger stability margin, a better grid-connected current characteristic, and anti-interference capability for GCI-*LCL* under the weak grid. The proposed dual-current feedback control strategy provides another method in active damping, performance improvement, and optimized operation for GCI-*LCL* in the modern power grid.

References

[1] M. R. Dorostkar-Ghamsari, M. Fotuhi-Firuzabad, M. Lehtonen, and A. Safdarian, "Value of distribution network reconfiguration in presence of renewable energy resources," *IEEE Trans. Power Syst.*, vol. 31, no. 3, pp. 1879–1888, May 2016.

[2] J. G. de Matos, F. S. F. Silva, and L. A. D. S. Ribeiro, "Power control in ac isolated micro grids with renewable energy sources and energy storage systems," *IEEE Trans. Ind. Electron.*, vol. 62, no. 6, pp. 3490–3498, Jun. 2015.

[3] R. N. Beres, X. Wang, M. Liserre, F. Blaabjerg, and C. L. Bak, "A review of passive power filters for three-phase grid-connected voltage-source converters," *IEEE J. Emerging Sel. Top. Power Electron.*, vol. 4, no. 1, pp. 54–69, Mar. 2016.

[4] J. L. Agorreta, M. Borrega, J. López, and L. Marroyo, "Modeling and control of *N*-paralleled grid-connected inverters with LCL filter coupled due to grid impedance in PV plants," *IEEE Trans. Power Electron.*, vol. 26, no. 3, pp. 770–785, Mar. 2011.

[5] W. Wu, Y. He, T. Tang, and F. Blaabjerg, "A new design method for the passive damped LCL and LLCL filter-based single-phase grid-tied inverter," *IEEE Trans. Ind. Electron.*, vol. 60, no. 10, pp. 4339–4350, Oct. 2013.

[6] Y. Tang, P. C. Loh, P. Wang, F. H. Choo, and F. Gao, "Exploring inherent damping characteristic of LCL-filters for three-phase grid-connected voltage source inverters," *IEEE Trans. Power Electron.*, vol. 27, no. 3, pp. 1433–1443, Mar. 2012.

[7] R. N. Beres, X. Wang, F. Blaabjerg, M. Liserre, and C. L. Bak, "Optimal design of high-order passive-damped filters for grid-connected applications," *IEEE Trans. Power Electron.*, vol. 31, no. 3, pp. 2083–2098, Mar. 2016.

[8] A. Kouchaki and M. Nymand, "Analytical design of passive LCL filter for three-phase two-level power factor correction rectifiers," *IEEE Trans. Power Electron.*, vol. 33, no. 4, pp. 3012–3022, Apr. 2018.

[9] S. G. Parker, B. P. McGrath, and D. G. Holmes, "Regions of active damping control for LCL filters," *IEEE Trans. Ind. Appl.*, vol. 50, no. 1, pp. 424–432, Jan./Feb. 2014.

[10] X. Li, J. Fang, Y. Tang, X. Wu, and Y. Geng, "Capacitor-voltage feedforward with full delay compensation to improve weak grids adaptability of LCL-filtered grid-connected converters for distributed generation systems," *IEEE Trans. Power Electron.*, vol. 33, no. 1, pp. 749–764, Jan. 2018.

[11] Z. Xin, X. Wang, P. C. Loh, and F. Blaabjerg, "Grid-current-feedback control for LCL-filtered grid converters with enhanced stability," *IEEE Trans. Power Electron.*, vol. 32, no. 4, pp. 3216–3228, Apr. 2017.

[12] C. A. Busada, S. Gomez Jorge, and J. A. Solsona, "Full-state feedback equivalent controller for active damping in LCL-filtered grid-connected inverters using a reduced number of sensors," *IEEE Trans. Ind. Electron.*, vol. 62, no. 10, pp. 5993–6002, Oct. 2015.

[13] A. K. Balasubramanian and V. John, "Analysis and design of split-capacitor resistive inductive passive damping for LCL filters in grid-connected inverters," *IET Power Electron.*, vol. 6, no. 9, pp. 1822–1832, Nov. 2013.

[14] N. He *et al.*, "Weighted average current control in a three-phase grid inverter with an LCL filter," *IEEE Trans. Power Electron.*, vol. 28, no. 6, pp. 2785–2797, Jun. 2013.

[15] W. Yao, Y. Yang, X. Zhang, F. Blaabjerg, and P. C. Loh, "Design and analysis of robust active damping for LCL filters using digital notch filters," *IEEE Trans. Power Electron.*, vol. 32, no. 3, pp. 2360–2375, Mar. 2017.

[16] R. Peña-Alzola, M. Liserre, F. Blaabjerg, R. Sebastián, J. Dannehl, and F. W. Fuchs, "Systematic design of the lead-lag network method for active damping in LCL-filter based three phase converters," *IEEE Trans. Ind. Inform.*, vol. 10, no. 1, pp. 43–52, Feb. 2014.

[17] J. Kukkola and M. Hinkkanen, "State observer for grid-voltage sensorless control of a converter equipped with an LCL filter: Direct discrete-time design," *IEEE Trans. Ind. Appl.*, vol. 52, no. 4, pp. 3133–3145, Jul./Aug. 2016.
[18] G. Escobar, S. Pettersson, and C. N. M. Ho, "Control of single-phase inverter connected to the grid through an LCL filter," in *Proc. 38th Annu. Conf. IEEE Ind. Electron. Soc.*, 2012, pp. 3406–3411.
[19] D. Yang, X. Ruan, and H. Wu, "Impedance shaping of the grid-connected inverter with LCL filter to improve its adaptability to the weak grid condition," *IEEE Trans. Power Electron.*, vol. 29, no. 11, pp. 5795–5805, Nov. 2014.
[20] K. Umetani, T. Tera, and K. Shirakawa, "Novel magnetic structure of integrated differential-mode and common-mode inductors to suppress dc saturation," in *Proc. Int. Power Electron. Conf.*, Hiroshima, Japan, 2014, pp. 304–311.
[21] T. F. Wu, M. Misra, L. C. Lin, and Y. H. Huang, "A modified division-summation digital control for grid-connected inverter with wide inductance variation of LCL filter," in *Proc. IEEE Appl. Power Electron. Conf. Expo.*, Tampa, FL, USA, 2017, pp. 2781–2787.
[22] C. Bao, X. Ruan, X. Wang, W. Li, D. Pan, and K. Weng, "Step-by-step controller design for LCL-type grid-connected inverter with capacitor–current-feedback active-damping," *IEEE Trans. Power Electron.*, vol. 29, no. 3, pp. 1239–1253, Mar. 2014.
[23] D. Pan, X. Ruan, X. Wang, H. Yu, and Z. Xing, "Analysis and design of current control schemes for LCL-type grid-connected inverter based on a general mathematical model," *IEEE Trans. Power Electron.*, vol. 32, no. 6, pp. 4395–4410, Jun. 2017.
[24] X. Zhang, P. Chen, C. Yu, F. Li, H. T. Do, and R. Cao, "Study of a current control strategy based on multisampling for high-power grid-connected inverters with an LCL filter," *IEEE Trans. Power Electron.*, vol. 32, no. 7, pp. 5023–5034, Jul. 2017.
[25] M. Lu, X. Wang, P. C. Loh, F. Blaabjerg, and T. Dragicevic, "Graphical evaluation of time-delay compensation techniques for digitally controlled converters," *IEEE Trans. Power Electron.*, vol. 33, no. 3, pp. 2601–2614, Mar. 2018.
[26] D. Pan, X. Ruan, C. Bao, W. Li, and X. Wang, "Capacitor-current-feedback active damping with reduced computation delay for improving robustness of LCL-type grid-connected inverter," *IEEE Trans. Power Electron.*, vol. 29, no. 7, pp. 3414–3427, Jul. 2014.
[27] X. Wang, C. Bao, X. Ruan, W. Li, and D. Pan, "Design considerations of digitally controlled LCL-filtered inverter with capacitor- current-feedback active damping," *IEEE J. Emerging Sel. Top. Power Electron.*, vol. 2, no. 4, pp. 972–984, Dec. 2014.
[28] C. Chen, J. Xiong, Z. Wan, J. Lei, and K. Zhang, "A time delay compensation method based on area equivalence for active damping of an LCL-type converter," *IEEE Trans. Power Electron.*, vol. 32, no. 1, pp. 762–772, Jan. 2017.
[29] M. B. Saïd-Romdhane, M. W. Naouar, I. Slama-Belkhodja, and E. Monmasson, "Robust active damping methods for LCL filter-based grid-connected converters," *IEEE Trans. Ind. Electron.*, vol. 32, no. 9, pp. 6739–6750, Sep. 2017.
[30] F. Liu, X. Zhang, C. Yu, Z. Shao, W. Zhao, and H. Ni, "LCL-filter design for grid-connected three-phase PWM converter based on maximum current ripple," in *Proc. IEEE ECCE Asia Downunder*, Melbourne, Vic., Australia, 2013, pp. 631–635.
[31] D. Pan, X. Ruan, C. Bao, W. Li, and X. Wang, "Optimized controller design for LCL-type grid-connected inverter to achieve high robustness against grid-impedance variation," *IEEE Trans. Ind. Electron.*, vol. 62, no. 3, pp. 1537–1547, Mar. 2015.
[32] M. Sanatkar-Chayjani and M. Monfared, "Design of LCL and LLCL filters for single-phase grid connected converters," *IET Power Electron.*, vol. 9, no. 9, pp. 1971–1978, Jul. 2016.

Yuanpeng Guan was born in Hainan, China, in 1992. He received the B.S. degree in electrical engineering from the Huazhong University of Science and Technology, Wuhan, China, in 2014, and the M.S. degree in power electronic in 2017 from the South China University of Technology, Guangzhou, China, where he has been working toward the Ph.D. degree in power electronic at the School of Electric Power, since 2017.

His current research interests include grid-connected inverters and dual-active-bridge dc–dc converters.

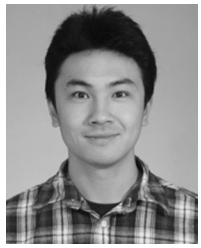

Yu Wang was born in Guangdong, China, in 1984. He received the B.S. degree in electronic engineering from Nanchang Hangkong University, Nanchang, China, in 2007, the M.S. degree in control engineering from Guangxi University, Nanning, China, in 2010, and the Ph.D. degree in power electronics from the South China University of Technology, Guangzhou, China, in 2015.

From 2015 to 2017, he worked as a Postdoctoral Researcher with the Department of Electrical Engineering, Tsinghua University, Beijing, China. He is currently an Associate Professor with the School of Automation, Guangdong University of Technology, Guangzhou. His current research interests include power electronic converters and flexible dc transmission and distribution systems.

Yunxiang Xie was born in Hunan, China, in 1965. He received the B.S., M.S., and Ph.D. degrees in electrical engineering from Xi'an Jiaotong University, Xi'an, China, in 1985, 1988, and 1991, respectively.

Since 1991, he has been with the School of Electric Power, South China University of Technology, Guangzhou, China, where he is currently working as a Professor. His current research interests include energy and power quality.

Yi Liang was born in Guangdong, China, in 1993. He received the B.S. degree in electrical engineering from the Southwest Jiaotong University, Chengdu, China, in 2016. Since 2016, he has been working toward the M.S. degree in power electronics at the School of Electric Power, South China University of Technology, Guangzhou, China.

His current research interests include photovoltaic inverters and dual-active-bridge dc–dc converters.

Anna Lin was born in Guangdong, China, in 1995. She received the B.S. degree in electrical engineering from the Beijing Jiaotong University, Beijing, China, in 2017. Since 2017, she has been working toward the M.S. degree in power electronic at the School of Electric Power, South China University of Technology, Guangzhou, China.

Her current research interest focuses on the photovoltaic inverters.

Xuemei Wang (M'12) received the M.Sc. degree in control engineering from Central South University, Changsha, China, in 2004, and the Ph.D. degree in power electronics and power drives from South China University of Technology, Guangzhou, China, in 2009.

Since 2009, she has been with the School of Electric Power, South China University of Technology, where she is currently working as a Professor. Her current research interests include intelligent modeling and control, reliability and state monitoring of power modules, and nonlinear behavior of power converters.